Sensitivity Studies in a Two-Dimensional Atmospheric Transport Model

J.V. Mansbridge and I.G. Enting

C S I R O
AUSTRALIA

Sensitivity Studies in a Two-Dimensional Atmospheric Transport Model

by J.V. Mansbridge and I.G. Enting

Division of Atmospheric Research Technical Paper No. 18

CSIRO
AUSTRALIA

Sensitivity Studies in a Two-Dimensional Atmospheric Transport Model

J.V. Mansbridge and I.G. Enting
CSIRO, Division of Atmospheric Research
Private Bag 1, Mordialloc, Vic 3195, Australia

Abstract

This report describes a series of sensitivity studies carried out on a two-dimensional atmospheric transport model. The model was used to deduce sources of total carbon given surface observations of CO_2. It was found that the deduced sources are very sensitive to the vertical resolution in the model if the procedure used to specify the lower boundary condition and deduce the tracer source is only accurate to first order in the vertical grid spacing. A number of improved formulations of this lower boundary condition are suggested and tested.

1. Introduction

In a recent paper (Enting and Mansbridge, 1989, hereinafter called EM3) we attempted to calculate the zonally averaged net source of total carbon for the atmosphere. Figure 1 shows this deduced source as a function of time and latitude. (This is the same as Figure 1 in EM3.)

The result was found by employing surface observations of carbon dioxide as the lower boundary conditions of a global, two-dimensional transport model. The 2-d model is fully described in Enting and Mansbridge, 1986 (hereinafter called EM1), some preliminary studies with the model are described in Enting and Mansbridge, 1987 (hereinafter called EM2) and the surface observations are described in EM3.

In this paper we investigate the dependence of the deduced source upon individual features of the source-deduction method. We consider the importance of

1) the horizontal and vertical resolution in the model,

2) the treatment of the lower boundary condition,

3) the size of the time step in the numerical integration,

4) uncertainties in the surface carbon dioxide observations,

5) uncertainties in the zonally averaged transport coefficients,

6) errors in the projection of the transport coefficients onto the time and space grids.

Each of these features is studied by comparing the standard result in Figure 1 to the corresponding result from a perturbed integration.

The standard run has 8 vertical levels equally spaced in pressure and 10 equal area horizontal zones. A time step of 0.001 years is used for the integration and this
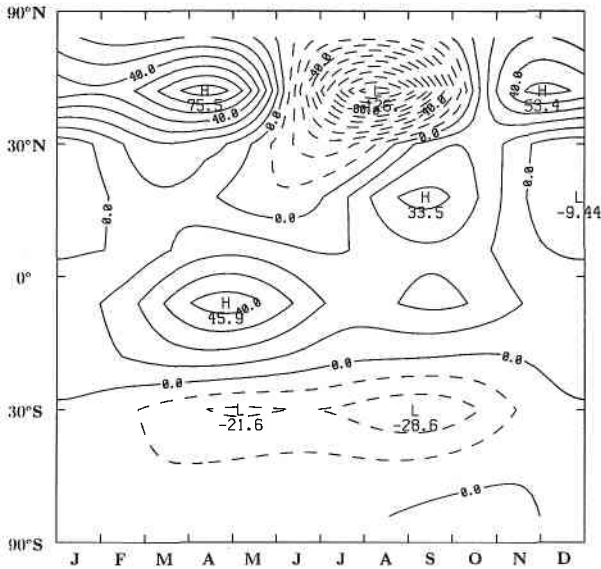
Figure 1: Deduced source of total carbon in the standard run as a function of sine(latitude) and time. Units are Gigatonnes of carbon per year per unit area (the total surface area of the earth taken as 1).

is close to the limit for numerical stability. The surface CO_2 observations are taken as strictly periodic seasonal cycles at all latitudes superimposed on a fixed inter-hemispheric gradient and a linear concentration increase of 1.5 ppmv yr^{-1} that is the same at all sites. The seasonal cycle and inter-hemispheric gradient are expressed as a Fourier series in space and time, the coefficients of which are given in Table 1 of EM3. That paper also describes the pseudo-Lagrangian transport fields that are used in the model (originally derived from a 3-d General Circulation Model by Plumb and Mahlman, 1987) .

It should be noted that the deduced source in each run was found by running the 2-d model in source-deduction mode for 3 years of model time starting from uniform initial conditions. The deduced source in the figures actually refers to the source in the third year. Integrations over a fourth year have shown that the solution is almost exactly periodic by this time.

2. Horizontal and vertical resolution

In Section 4 of EM2 it was shown that horizontal and vertical resolution have only a small effect upon the model transport of a passive tracer (CCl_3F). However, the deduction of the carbon source, being an inverse problem (Newsam and Enting, 1988), would be expected to be more sensitive to any variation in the specification of the integration. Accordingly, we carried out a number of runs varying the horizontal and/or vertical resolution. (Of course it was also necessary to change the time step in accordance with the stability criterion — see EM1.) Table 1 lists some statistics which allow the comparison between the deduced source in these runs and the

	10	20	30
8	(1.000, 0.00, 1.00)	(0.995, 2.70, 1.01)	(0.993, 3.13, 1.02)
16	(0.994, 3.65, 0.89)	(0.992, 3.87, 0.90)	
24	(0.990, 5.23, 0.83)		

Table 1: Statistics comparing CO_2 sources determined from runs with NH horizontal zones (listed across the top row) and NV vertical levels (listed down the first column) to the standard run (with NH = 10 and NV = 8). In each triplet the first number is the correlation coefficient, the second number is the root mean square error $(Gt/(E^*yr))$ and the third number is the regression coefficient.

deduced source in the standard run.

The table contains triplets of numbers relating to runs with various combinations of NV, the number of levels in the vertical, and NH, the number of zones in the horizontal. The first number of each triplet is the sample correlation coefficient, r, between the deduced source in the given run and the standard deduced source. The correlation coefficient is defined, for example, by Hoel (1971) and is calculated by summing over points in space-time. There are usually 10 grid points in the horizontal and 100 points in time spaced 0.01 years apart. (In runs where NH = 20 or 30 then adjacent zones are combined to give 10 'equivalent' zones.)

The second number in each triplet is the root mean square error, rmse, calculated over the same points in space-time. The units are Gigatonnes of carbon per unit area per year $(Gt/(E^*yr))$, where the unit area has been normalized to the Earth's surface.

The third number is the coefficient a which gives the least squares best fit to the equation $y = a x$. Here x is the vector of source values for the standard run at the 1000 space-time points and y is the corresponding vector for the perturbed run.

Table 1 shows that as NH increases the correlation coefficient decreases, the root mean square error increases and the regression coefficient increases slightly. Figure 2 shows the deduced source when NH = 30. The source is shown for each of the 30 zones and so has more sharply defined peaks than the standard source in Figure 1. If neighbouring zones are combined to produce sources for the 10 standard zones then the corresponding plot is very similar to the standard source in Figure 1. This is to be expected since the regression coefficient changes only slightly with NH and so indicates that increasing NH does not systematically change the deduced source in the 10 standard zones.

In contrast, increasing NV significantly changes the deduced source. Figure 3, in which NV = 24, shows much smaller peaks and troughs than the standard source in Figure 1 although the two sources are very similar in shape. This is borne out by the correlation and regression coefficients in Table 1. These show that as NV increases the correlation coefficient decreases slightly but the regression coefficient decreases significantly.

This systematic behaviour occurs because the numerical scheme for combining source-deduction and boundary value specification is only accurate to first order. This is demonstrated in the next section where we also suggest improved methods of specifying the boundary condition, and thereby deducing the source.
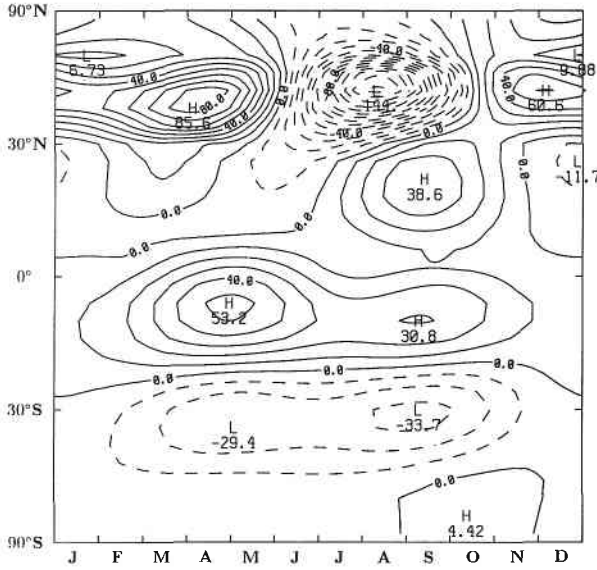
Figure 2: As for Figure 1, but with 30 latitudinal zones (NH = 30) instead of 10 and DT = 0.0001 years to ensure stability.
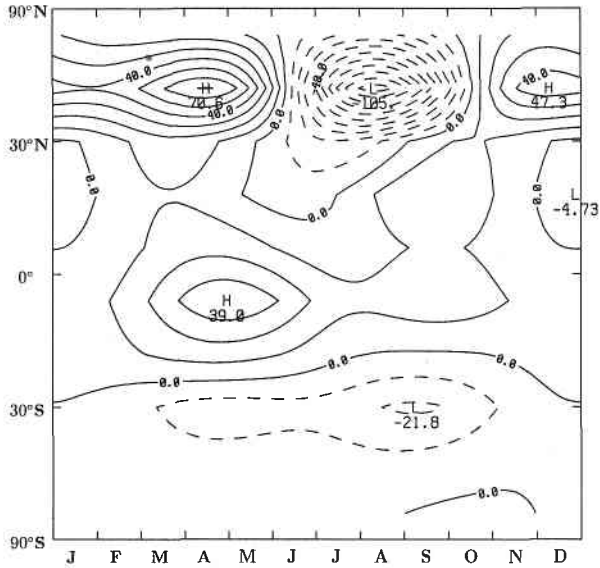

Figure 3: As for Figure 1, but with 24 vertical levels (NV = 24) instead of 8 and DT = 0.000075 years to ensure stability.

3. The lower boundary condition

The strong dependence of the deduced source upon the vertical resolution may be understood by studying a simplified version of the transport equations. Consider the one-dimensional diffusion equation for the tracer concentration $C(z,t)$

$$\frac{\partial C}{\partial t} = K \frac{\partial^2 C}{\partial z^2}, \tag{1}$$

where z is the vertical coordinate and t is time. To simplify the analytical solution the top of the atmosphere is at $z = 0$ and the surface is at $z = 1$. The boundary conditions are

$$\left. \frac{\partial C}{\partial z} \right|_{z=0} = 0 \tag{2a}$$

and

$$C(1,t) = \Re \left(C_s e^{i\omega t} \right). \tag{2b}$$

These boundary conditions enforce symmetry at one boundary (or, equivalently, zero tracer flux) and a sinusoidal observed field at the other boundary.

Consistent with the diffusion equation the deduced surface source is given by

$$S(t) = K \left. \frac{\partial C}{\partial z} \right|_{z=1}. \tag{3}$$

The above problem has the analytical solution

$$C(z,t) = \Re \left(C_\omega(z) e^{i\omega t} \right), \tag{4}$$

where

$$C_\omega(z) = C_s \cosh(\alpha z) / \cosh(a) \tag{5a}$$

and

$$i\omega = K\alpha^2. \tag{5b}$$

The deduced source is then

$$S(t) = \Re \left(S_\omega e^{i\omega t} \right), \tag{6}$$

where

$$S_\omega = K\alpha C_s \tanh(\alpha). \tag{7}$$

The solution is then characterized by the ratio of the deduced source to the observed surface concentration, namely,

$$S_\omega / C_s = K\alpha \tanh(\alpha). \tag{8}$$

We now investigate how different methods of numerical solution to the above problem will depend differently upon the vertical resolution. Equation (1) is approximated by

$$\frac{\partial C_j}{\partial t} = \frac{K}{\Delta^2} (C_{j+1} + C_{j-1} - 2C_j), \quad \text{for} \quad j = 2, N-1, \tag{9}$$

where the vertical direction has been divided into N levels. Here $\Delta = 1/N$ and C_j refers to the concentration at the centre of the jth level, i.e., at $z = (j - 0.5)/N$. This equation has the solution

$$C_j = \Re\left(C_{\omega,j} e^{i\omega t}\right), \tag{10}$$

where

$$C_{\omega,j} = \gamma\left(a^j + a^{-j}\right), \tag{11a}$$

and a is found from the equation

$$a^2 - \left[\frac{i\omega\Delta^2}{K} + 2\right]a + 1 = 0. \tag{11b}$$

Note that, according to eq. 11a, $C_{\omega,-1} = C_{\omega,+1}$ and so the symmetry boundary condition (eq. 2a) is satisfied. The variable γ is found, in principle, by applying the second boundary condition, (eq. 2b). First, observe that the rate of change of the tracer concentration in the Nth layer is given by the sum of the flux through the lower boundary (the source) and the flux through the top of that layer. Thus

$$\Delta\frac{\partial C_N}{\partial t} = \frac{K}{\Delta}\left(C_{N-1} + C_N\right) + S(t). \tag{12}$$

Using eqs. 10 and 11a we may be rewrite eq. 12 as

$$AC_{\omega,N} = S_\omega, \tag{13}$$

where

$$A = i\omega\Delta + \frac{K}{\Delta}(1 - R) \tag{14a}$$

and

$$R = \frac{a^{N-1} + a^{1-N}}{a^N + a^{-N}} \tag{14b}$$

The finite difference problem may now be solved after defining the source-deduction method. In the standard source-deduction method used in the 2-d transport model (and in EM3 in particular) the tracer concentration in the bottom layer, $C_{\omega,N}$, is simply replaced by observed surface concentration, C_s. Thus, eq. 13 gives

$$S_\omega/C_s = A. \tag{15}$$

This value of the ratio of deduced source to surface concentration should be compared to the corresponding ratio for the solution to the original partial differential equation (given by eq. 8). The absolute value of the relative difference between the two estimates of the ratio is given by

$$(\text{relative error})_1 = \left|1 - \frac{A}{K\alpha}\tanh\alpha\right|. \tag{16}$$

The solid curve in Figure 4 shows this relative error as a function of N, the number of grid points. The diffusion coefficient $K = 0.3045$. This is the lower
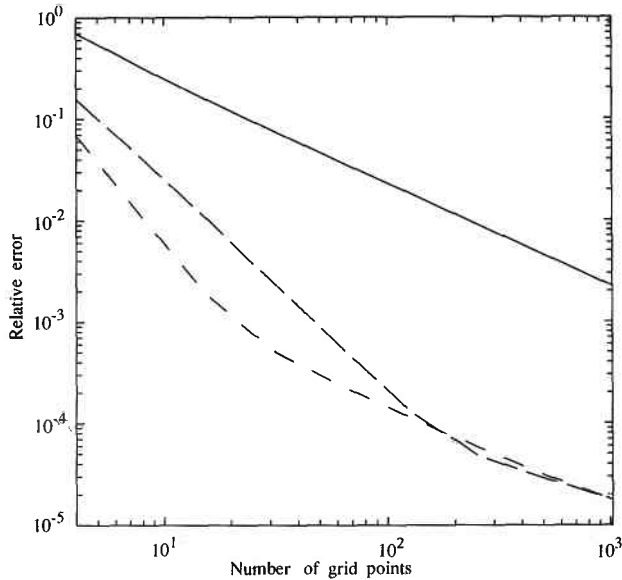
Figure 4: Relative error in the ratio of deduced source to surface tracer value for $K = 0.3045$ in the one-dimensional diffusion system, given as a function of the number of grid points. The solid curve refers to the standard source-deduction method, the broken curve refers to the linear approximation to the tracer gradient and the dashed curve refers to the quadratic approximation to the tracer gradient.

limit of the non-dimensionalized vertical diffusion coefficient which was used in the standard run of the 2-d model. It is appropriate to use this lower limit (which corresponds to 0.5 metre^2 sec^{-1}) because the vertical eddy diffusion coefficient takes this value on the lower boundary of the 2-d model. The frequency is $\omega = 2\pi$ because the annual cycle is the strongest cycle in the real atmosphere.

The relative error is approximately 32% when there are 8 levels in the vertical and has only dropped to 10% for the 24 level model. (Note the logarithmic scale.) Choosing the minimum possible value of the diffusion coefficient probably overestimates the relative error in the standard run of the 2-d model, however the relative error decreases only slowly as a function of K. The solid curve in Figure 5 shows how the relative error depends on K. Even for a non-dimensional value of 3.0 (5.1 metre^2 sec^{-1}) the relative error is still greater than 8%. It appears that these errors are large enough to explain the strong dependence of the deduced source upon vertical resolution in the 2-d model (see, for example, Table 1).

This resolution dependence is clearly undesirable and so a number of other source-deduction methods were examined. Recalling eq. 3, the tracer gradient at the surface may be approximated by the gradient between the centre of the box and the surface. Thus

$$S_\omega = \frac{2K}{\Delta} \left(C_s - C_{\omega,N} \right) \tag{17}$$
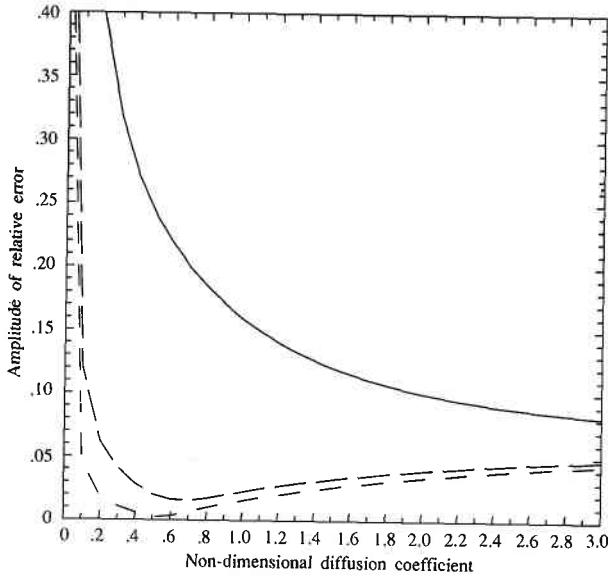
Figure 5: Relative error in the ratio of deduced source to surface tracer value as a function of the diffusion coefficient when there are 8 grid points. The solid curve refers to the standard source-deduction method, the broken curve refers to the linear approximation to the tracer gradient and the dashed curve refers to the quadratic approximation to the tracer gradient.

may be used to eliminate $C_{\omega,n}$ in eq. 13 to give

$$\frac{S_\omega}{C_s} = \frac{a}{1 + A\Delta/2K}. \tag{18}$$

The relative error for this method is plotted on Figures 4 and 5 as the broken curves. Even for a few as 8 levels the relative error is only 4% for $K = 0.3045$.

The third source-deduction method to be examined attempts to find the tracer gradient at the surface by fitting a parabola between C_N, C_{N-1} and C_s. (The second method fitted a straight line between C_N and C_s.) This gives

$$\frac{S_\omega}{C_s} = \frac{K}{\Delta} \left(8C_s/3 - 3C_N + C_{N-1}/3 \right), \tag{19}$$

and thus

$$\frac{S_\omega}{C_s} = \frac{8A}{3\Delta A/K + 9 - R}. \tag{20}$$

The relative error resulting from this approximation is shown as the dashed curves in Figures 4 and 5. The method has the smallest errors of all with a relative error of only 1% for the 8 level model at $K = 0.3045$.

This last approximation has been tested in some preliminary runs of the 2-d model and has been found to be stable. These experiments have also indicated that the above calculations are broadly applicable to the 2-d model. When the
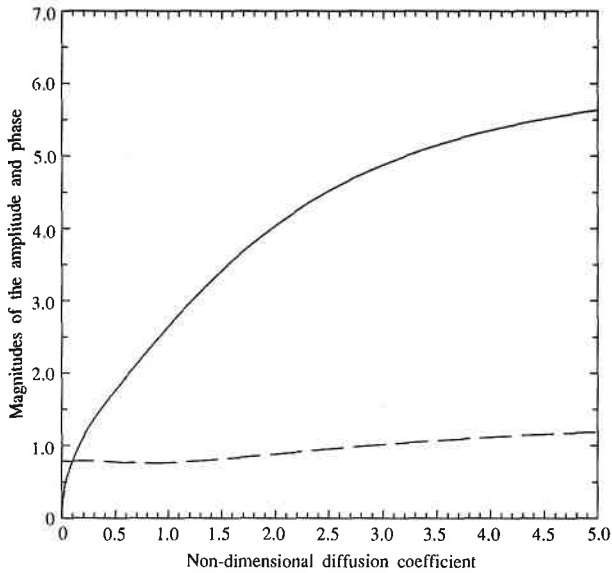
Figure 6: Amplitude (solid curve) and phase (broken curve) in the ratio of deduced source to surface tracer value as a function of the diffusion coefficient.

third source deduction method is used the sources are not as strongly dependent on vertical resolution as are the sources using the standard deduction method. Also, when the new method is employed the deduced sources for NV = 8 and 24 more closely resemble the sources found by the standard method's NV = 24 version than its NV = 8 version. Given these observations it is useful to consider briefly the physical interpretation of the different source-deduction methods.

The standard source-deduction method is strongly dependent on the vertical resolution because the tracer concentration in the lowest level is set equal to the observed surface concentration. This would not cause a very large error if the transport fields used in the 2-d model were consistent with a well mixed boundary layer of depth $> \Delta$. This boundary layer depth will be $O\left(\sqrt{K/\omega}\right) = 0.05$ in non-dimensional height for $K = 0.3045$ and $w = 2\pi$. Thus, as can also be seen from Figure 4, more than 20 vertical levels are required before the approximation produces acceptably small errors.

However, even much higher vertical resolutions will not necessarily produce an acceptable solution. Consider Figure 6 which shows how the function S_ω/C_s depends on K. For large values of K, $|S_\omega/C_s|$ asymptotes to 2π but for small values it changes rapidly. If $K = 0.3045$ then $\frac{d}{dK}|S_\omega/C_s| = 2.21$. Thus, for a given set of observations, doubling K will quadruple the magnitude of the deduced source. Even if $K = 3.0$ then $\frac{d}{dK}|S_\omega/C_s| = 0.62$. For the standard source-deduction method the value of K is taken simply as the value at the top of the layer closest to the surface and this will reach the lower bound of K for a sufficiently great vertical resolution.

Rather than use such an ad hoc method to characterize the flux through the surface boundary layer it seems preferable to use a direct model such as one of the alternatives already discussed. This need to accurately parameterize the boundary
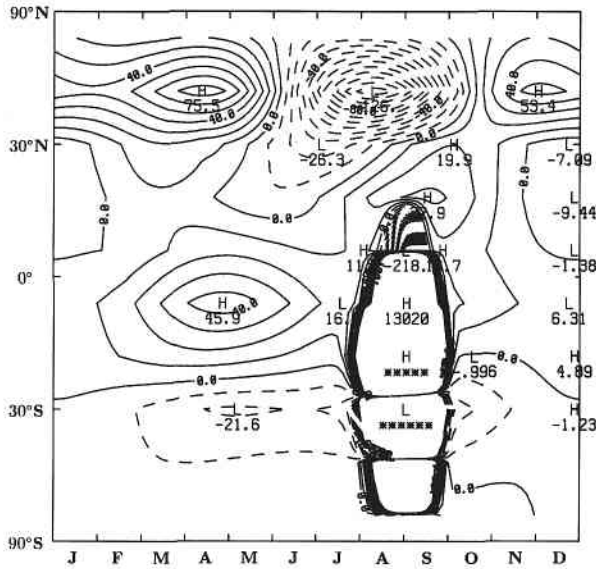
Figure 7: As for Figure 1, but with DT = 0.0011 years instead of 0.001 to give numerical instability.

layer of the real atmosphere is a severe limitation on the modelling of the atmospheric transport.

4. Time step dependence

The stability of the time stepping scheme used in the numerical integration is discussed in detail in Section 5 of EM1. Equation 5.12 in that paper states the effective upper bound of time step DT. In the standard integration we use DT = 0.001 years. This is very close to producing an unstable integration for, as Figure 7 shows, setting DT = 0.0011 years results in a spurious source/sink term after the middle of the year.

Nevertheless, this solution is very similar to the standard solution before the instability appears. The two integrations can be compared in a number of ways. The pattern correlation coefficient r, is 0.999996 for the first half of the year (only the first 50 time points are used for the correlation). Also the rmse is only 0.06352 Gt/(E*yr)for the first half of the year.

The insensitivity of the deduced source to the time step is further illustrated by carrying out an integration with DT = 0.0005 years. The time-latitude plot of the deduced source is not shown here because it is indistinguishable from that of the standard case shown in Figure 1. For the full year the pattern correlation coefficient is $r = 0.999999$ and the root mean square error is rmse = 0.01718 Gt/(E*yr).

Thus, we conclude that the integration is unaffected by the size of the time step provided that the time step satisfies the stability criteria. It therefore seems unnecessary to use more sophisticated, but computationally expensive, time-stepping schemes such as the one employed by Tans et al. (1989).
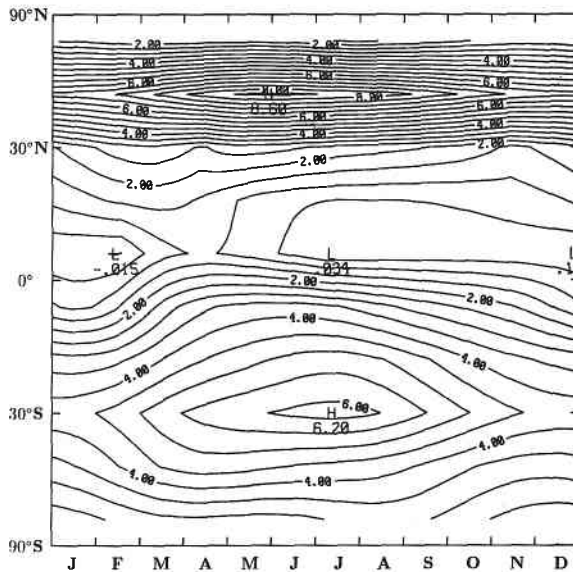
Figure 8: As for Figure 1, but the surface concentrations are solely a trend of 1.5 ppmv yr^{-1}.

5. Variation in the surface observations

Because we are dealing with an inverse problem we would expect the deduced surface source to be strongly influenced by errors in the observed surface concentrations. The deduced source depends linearly on the observations and so we can examine separately the three parts of the observations (the trend, seasonal variation and inter-hemispheric gradient). Note that, since the initial concentrations are set to zero everywhere, this linearity applies not just at steady state but at all times.

Figure 8 shows the deduced source when the surface concentrations are simply the trend of 1.5 ppmv yr^{-1}. The space-time structure of the deduced sources is entirely due to the space and time variations of the transport fields. The latitudinal structure of the annual mean deduced sources is shown in Figure 9. Here the strong apparent sources in the mid-latitudes are required to balance the transport due to the Hadley-cell circulation and so maintain equal CO_2 concentrations at all latitudes.

Because the deduced source depends linearly on the observations the errors involved in wrongly specifying the trend are easily estimated by rescaling Figure 8. The root mean square value of the source in the figure is 3.85 Gt/(E*yr). Thus, for example, an error in the trend of 0.2 ppmv yr^{-1}would cause a root mean square difference of 0.51 Gt/(E*yr).

Figure 10 shows the seasonal variation in the surface CO_2 observations for the standard run. The Fourier coefficients which specify this variation are given in Table 2. (The data set from which the coefficients are derived is given in Table 3 of EM2.) The accuracy of this estimate of the seasonal variation of surface CO_2 may be guessed by using the same method to derive a new estimate from a different
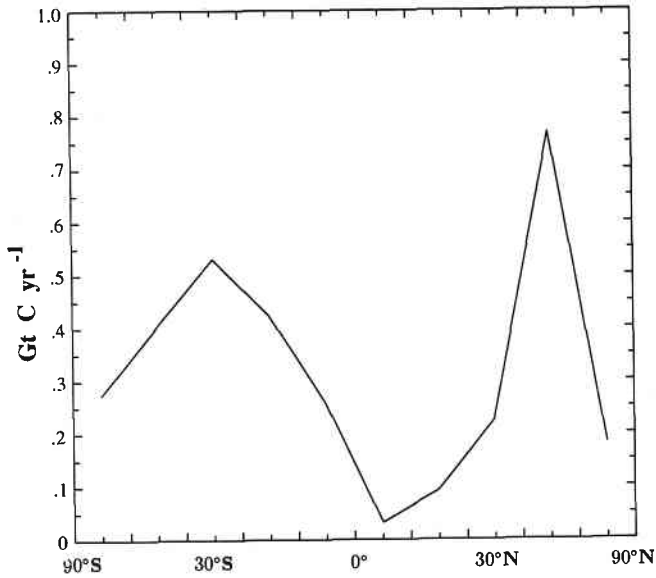
Figure 9: Total annual carbon sources (in Gigatonnes) in each of 10 equal area latitudinal zones where the surface concentrations are solely a trend of 1.5 ppmv yr^{-1}.
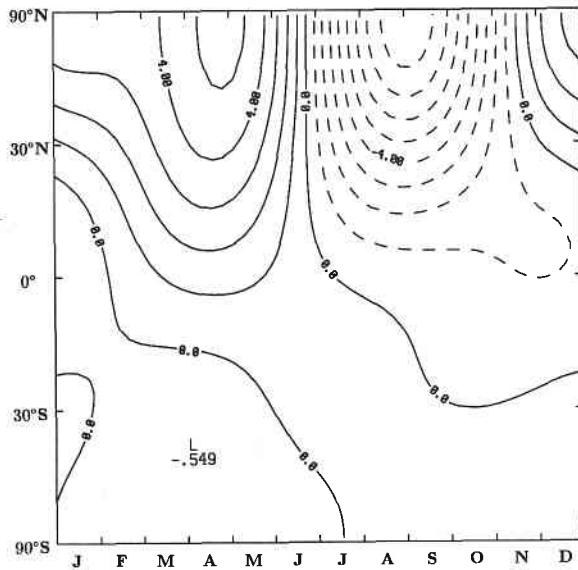

Figure 10: The contribution to the surface CO_2 observations made by the seasonal cycle used in the standard run.

	$\cos(2\pi t)$	$\sin(2\pi t)$	$\cos(4\pi t)$	$\sin(4\pi t)$
1	0.334	1.810	-0.107	-0.636
$\cos(\pi x)$	-0.865	-3.054	-0.220	1.058
$\cos(2\pi x)$	0.850	0.819	0.415	-0.553
$\cos(3\pi x)$	-0.264	-0.148	-0.401	0.085

Table 2: Coefficients describing the seasonal variation of CO_2 concentration in the standard run.
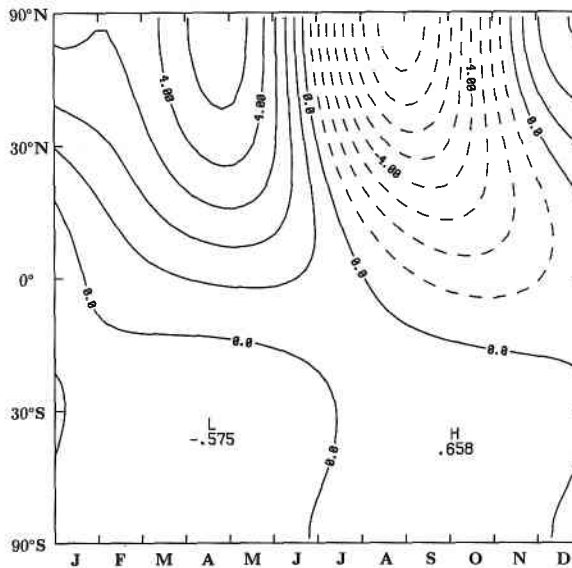

Figure 11: The contribution to the surface CO_2 observations made by the seasonal cycle derived from GMCC data (Harris and Bodhaine, 1983).

data set (Harris and Bodhaine, 1983). The resultant seasonal variation is shown in Figure 11. The corresponding Fourier coefficients are given in Table 3. The pattern correlation coefficient for the two figures is 0.986, the root mean square difference is 0.404 ppmv and the linear regression of the new set of seasonal observations against the standard set gives a coefficient of 1.023.

The corresponding deduced sources from the two data sets are given in Figures 12 and 13. The pattern correlation coefficient is 0.964, the root mean square difference between the two figures is 6.49 $Gt/(E^+ yr)$ and the linear regression coefficient is 1.085. The inversion process has accentuated the difference between the two observational sets with the most significant change being in the magnitude of the small source/sink pair at around 30°S. This suggests that this feature may be within the noise level of the data. The noisiness of the inversion in the Southern Hemisphere is further emphasized by Figure 14 which shows the annual mean of the deduced source. It should be realised however that the seasonal variation in CO_2 concentration makes a relatively small contribution to the estimated annual mean source in the Southern Hemisphere. The dominant contributions are from the trend

	$\cos(2\pi t)$	$\sin(2\pi t)$	$\cos(4\pi t)$	$\sin(4\pi t)$
1	0.275	1.880	0.251	-0.622
$\cos(\pi x)$	-0.753	-3.256	-0.394	1.101
$\cos(2\pi x)$	0.876	0.700	0.076	-0.659
$\cos(3\pi x)$	-0.507	0.223	0.010	0.202

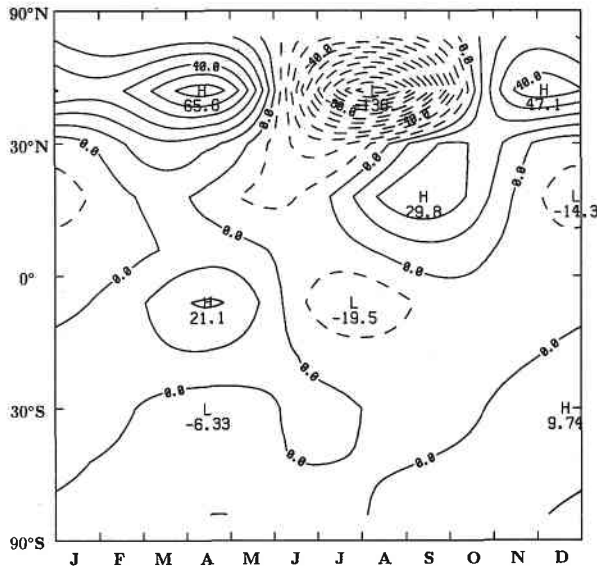Table 3: Coefficients describing the seasonal variation of CO_2 derived from the GMCC data set.

Figure 12: As for Figure 1, but the surface concentrations are the seasonal cycle from the standard run.
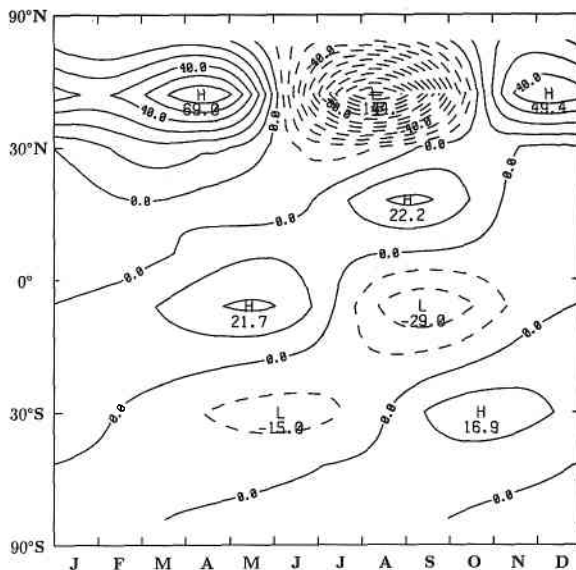
Figure 13: As for Figure 1, but the surface concentrations are the seasonal cycle derived from GMCC data (Harris and Bodhaine, 1983).

and inter-hemispheric gradient.

The deduced source associated with the inter-hemispheric gradient of CO_2 was studied by using four different estimates. These four estimates, which are shown superimposed in Figure 15, were derived by applying the same method to different data sets. A finite Fourier cosine series in $x = 0.5(1 + \sin(\text{latitude}))$ was fitted to the data by a least squares technique. The constant coefficient was then neglected as it must be absorbed by the trend term. Table 4 gives the resultant sets of Fourier coefficients.

Coefficient set A is used in the standard run and was derived from the annual mean data of Harris and Bodhaine (1983) normalized to 1982. Set B was derived in the same way, and from the same data, but involves fitting only the first four

Set	$\cos(\pi x)$	$\cos(2\pi x)$	$\cos(3\pi x)$	$\cos(4\pi x)$	$\cos(5\pi x)$
A	-1.490	-0.294	0.134	0.338	-0.115
B	-1.490	-0.196	0.032		
C	-1.258	0.004	-0.111	0.179	-0.000
D	-1.370	-0.010	-0.160	0.142	0.134

Table 4: Coefficients describing the inter-hemispheric gradient of CO_2. Coefficient set A is used in the standard run and was derived from the annual mean data of Harris and Bodhaine (1983) normalized to 1982. Set B was derived from the same data but involves a least squares fit to only the first three Fourier components. Set C was derived using only the 1982 annual mean data of Harris and Bodhaine. Data set D is derived from the GMCC 1984 annual means (Schnell and Rosson, 1986).
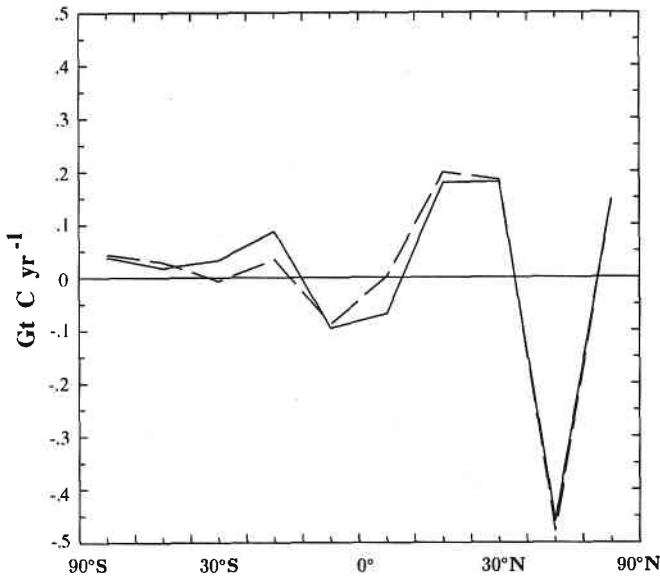
Figure 14: Total annual carbon sources (in Gigatonnes) in each of 10 equal area latitudinal zones. The solid curve is for the case where the surface CO_2 observations are taken from the seasonally varying part of the standard surface observations (Figure 10) and the broken curve is for the case where the alternative seasonal variation is used (Figure 11).

Fourier components. For set C the data used were the 1982 annual means of CO_2 at 15 surface sites (again taken from Harris and Bodhaine, 1983). Data set D is derived from GMCC 1984 annual means at the same 15 surface sites (Schnell and Rosson, 1986).

Taken together these curves indicate the possible variation in estimates of the inter-hemispheric gradient. It should be realised that while curves A and B attempt to represent a composite year, curves C and D are smoothed versions of the gradient for particular years.

The year to year variability can be seen in Figure 16 which shows the finite Fourier approximation to the inter-hemispheric gradient for each of the years 1979 to 1985. The data are taken from Schnell and Rosson (1986). The curves for years 1981 to 1985 are from a 6 parameter fit to 15 surface stations while for 1979 and 1980 a 4 parameter fit was used because less surface data were available (there were 9 and 12 sites respectively). The inter-annual variability of the inter-hemispheric gradient appears to be of the same order as the variability between the 4 curves shown in Figure 15. It should be noted however that the latitudinal variation is much smoother for the years 1982 to 1985 (shown as continuous curves) than for the years 1979 to 1981 (shown as broken curves). It is most likely that this is due to improvements in the representativeness of the measurements. Hence the envelope of the four continuous curves is probably a good description of the inter-annual variability.

Set	B	C	D
A	(0.969, 0.11, 1.01)	(0.961, 0.14, 1.18)	(0.942, 0.15, 1.06)
B		(0.976, 0.11, 1.15)	(0.973, 0.10, 1.05)
C			(0.994, 0.05, 0.91)

Table 5: Statistics comparing the four approximations to the inter-hemispheric CO_2 gradient. In each triplet the first number is the correlation coefficient, the second number is the root mean square error and the third number is the regression coefficient.
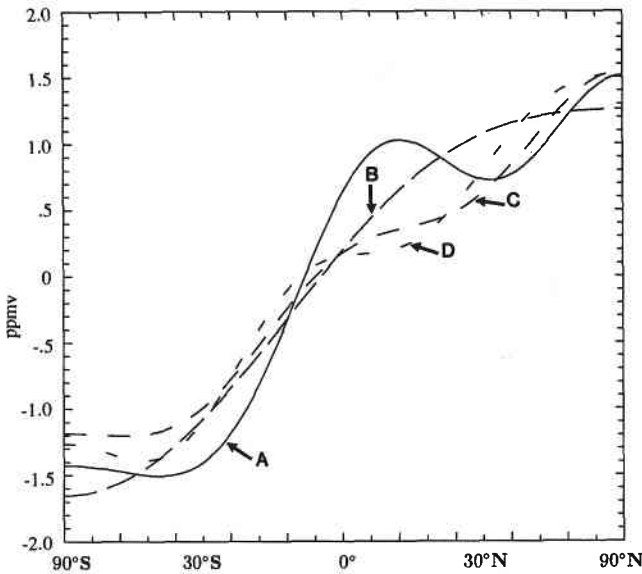

Figure 15: Different cosine series approximations to inter-hemispheric gradients of CO_2. Curve A is for the standard inter-hemispheric gradient, using a 6 term expansion. Curve B uses the same data as curve A but a 4 term expansion. Curve C uses a 6 term expansion to 1982 GMCC surface data. Curve D uses a 6 term expansion to 1984 GMCC surface data. The ordinate is $(1 + \sin(\text{latitude}))/2$ and the co-ordinate is in units of parts per million by volume (ppmv).

The four curves in Figure 15 are compared quantitatively in Table 5. For each pair of curves the table lists the pattern correlation coefficient, the root mean square difference and the linear regression coefficient. It should be noted that curves C and D do not resemble the standard curve (A) as closely as they resemble its lower resolution version (B). This is presumably because the non-surface data used in the determination of A and B were responsible for a significant amount of high frequency noise. Note also the strong correlation between curves C and D.

The triplets in Table 5 may be compared to those in Table 6, which shows the relationship between the deduced sources when curves A to D are used to specify the CO_2 observations. As would be expected from the the earlier table, the sources deduced from curve B more closely resemble those from curves C and D than do the sources from curve A. Also, the most highly correlated sources are those from
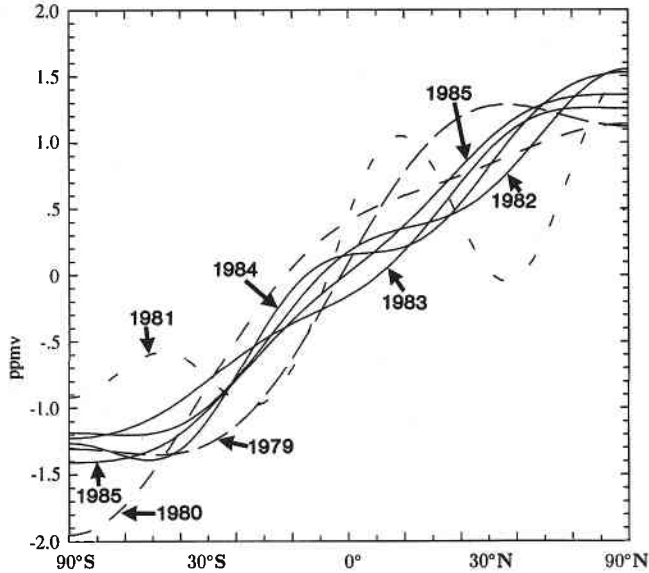
Figure 16: Cosine series approximations to inter-hemispheric gradients of CO_2 for the years 1979 to 1985. The ordinate is $(1 + \sin(\text{latitude}))/2$ and the co-ordinate is in units of parts per million by volume (ppmv). The data were taken from Schnell and Rosson, 1986.

Set	B	C	D
A	(0.793, 7.17, 1.30)	(0.856, 6.37, 1.37)	(0.692, 8.24, 0.85)
B		(0.940, 2.42, 0.91)	(0.903, 4.18, 0.68)
C			(0.949, 3.31, 0.73)

Table 6: Statistics comparing the four deduced sources resulting from the four approximations to the inter-hemispheric CO_2 gradient. In each triplet the first number is the correlation coefficient, the second number is the root mean square error and the third number is the regression coefficient.

curves C and D. All of the correlation coefficients in Table 6 are smaller than the corresponding ones in Table 5; this is because the inversion process causes 'errors' (in this case differences) to grow (EM3; Newsam and Enting, 1988).

These deduced sources are shown in Figures 17 to 20. They have similar time variations because the surface concentrations used to derive them differ only in their time independent parts. The differences caused by the different inter-hemispheric gradients are most obvious in Figure 21 which shows the annual mean values of the deduced sources for each of the curves. This Figure strongly suggests that the high frequency latitudinal variations in the standard inter-hemispheric gradient (curve A) have exaggerated the magnitude of the sink near 30°S and of the source near the equator. Also the deduced source in the Northern Hemisphere is noticeably different.

Figure 17: As for Figure 1, but the surface concentrations are the inter-hemispheric gradient as used in the standard run.

Figure 18: As for Figure 1, but the surface concentrations are the inter-hemispheric gradient formed from the 4 term cosine series expansion of the GMCC data used in the standard case.

Figure 19: As for Figure 1, but the surface concentrations are the inter-hemispheric gradient formed from the 6 term cosine series expansion to surface level GMCC 1982 annual mean data.

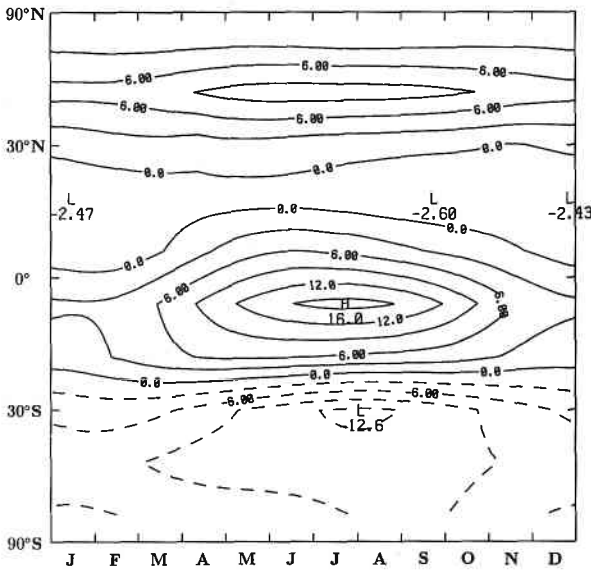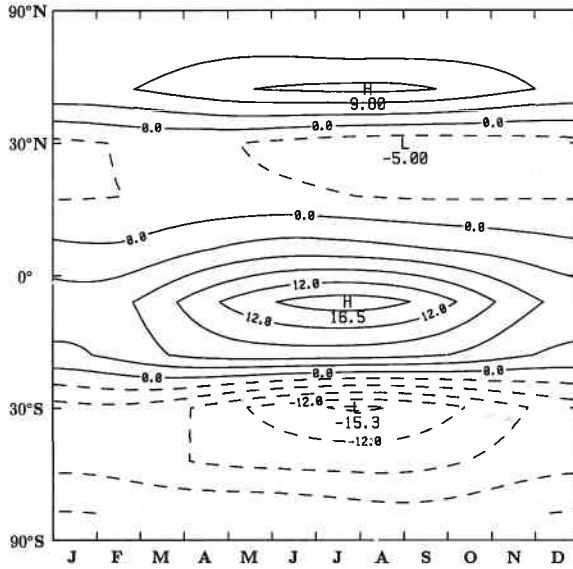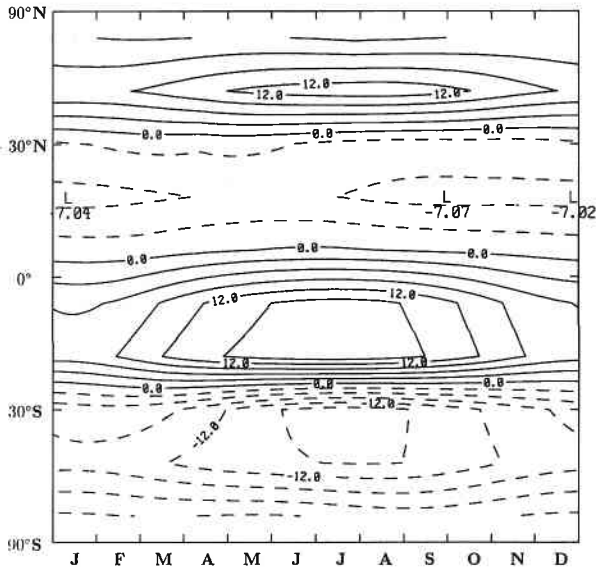

Figure 20: As for Figure 1, but the surface concentrations are the inter-hemispheric gradient formed from the 6 term cosine series expansion to surface level GMCC 1984 annual mean data.
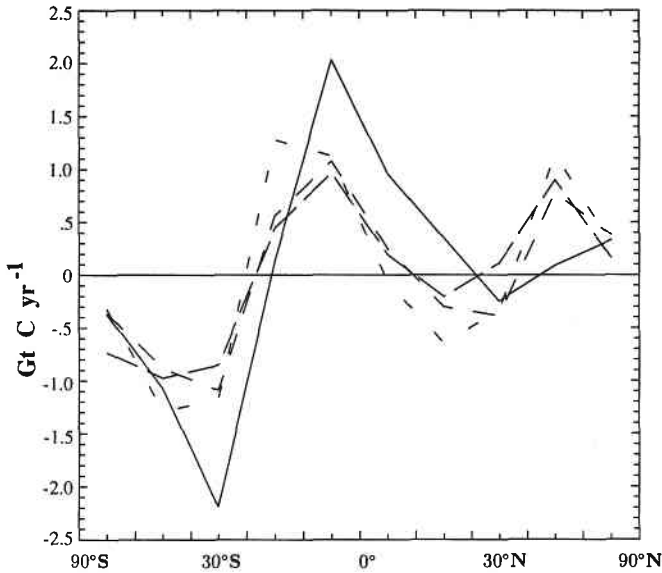
Figure 21: Total annual carbon sources (in Gigatonnes) in each of 10 equal area latitudinal zones. The four curves labelled A, B, C and D refer to the cases where the surface CO_2 concentrations are taken from the four descriptions of the inter-hemispheric gradient described in the text.

Set	β	γ
α	(0.968, 6.37, 1.03)	(0.938, 8.80, 0.95)
β		(0.965, 6.49, 0.92)

Table 7: Statistics comparing the deduced sources in three runs. The standard run is labelled α, the run with the curve C-type inter-hemispheric gradient is labelled β and the run with both the curve C-type inter-hemispheric gradient and the alternative seasonal cycle is labelled γ. Triplets are: (correlation coefficient, root mean square error, regression coefficient).

It should be noted that these results do not invalidate any of the conclusions in EM3. In that paper we stated that the weakness of the mid-latitude Southern Hemisphere sink compared to the mid-latitude Northern Hemisphere sink suggests that there are strong non-oceanic sinks in Northern latitudes; this conclusion would thus be strengthened by using one of the other inter-hemispheric gradients. Similarly, a weaker net equatorial source, but with the same seasonality, would not require the alteration of any of our discussion in EM3 (in particular, see Section 5.5 of EM3).

The total effect of errors in the surface CO_2 observations may be estimated by comparing Figure 1 (the standard deduced source) with Figures 22 and 23. The concentrations used in the derivation of Figure 22 differ from the standard ones by using the curve C inter-hemispheric gradient. Figure 23 uses the same inter-hemispheric gradient and the alternative seasonal cycle discussed earlier.
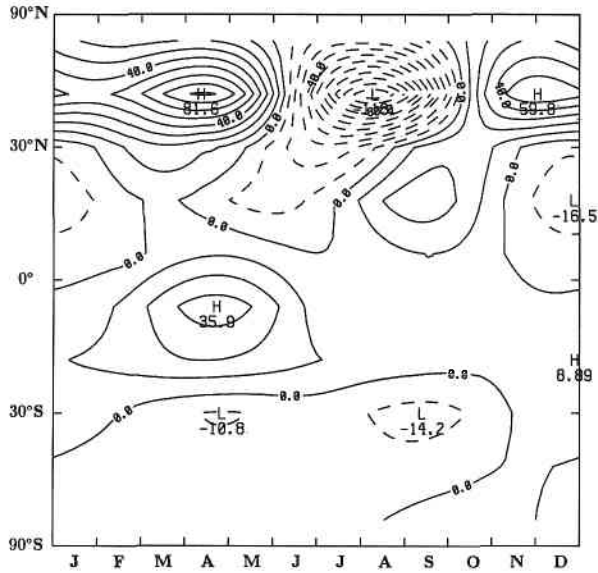
Figure 22: As for Figure 1, but the surface concentrations differ from the standard run by using the type C inter-hemispheric gradient.
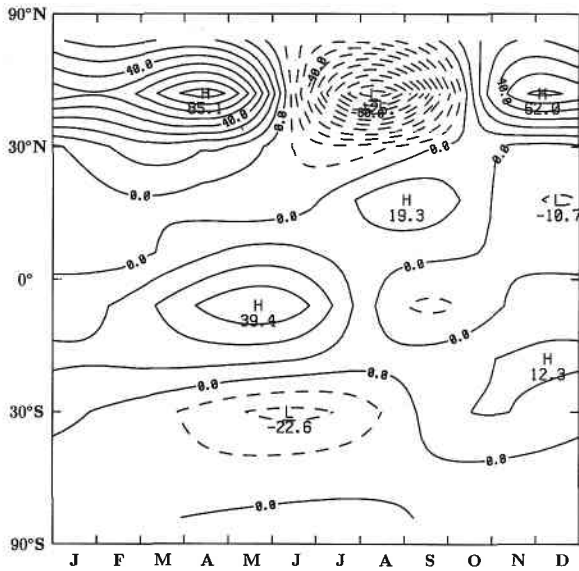

Figure 23: As for Figure 1, but the surface concentrations differ from the standard run by using the type C inter-hemispheric gradient and the alternative (GMCC) seasonal cycle.
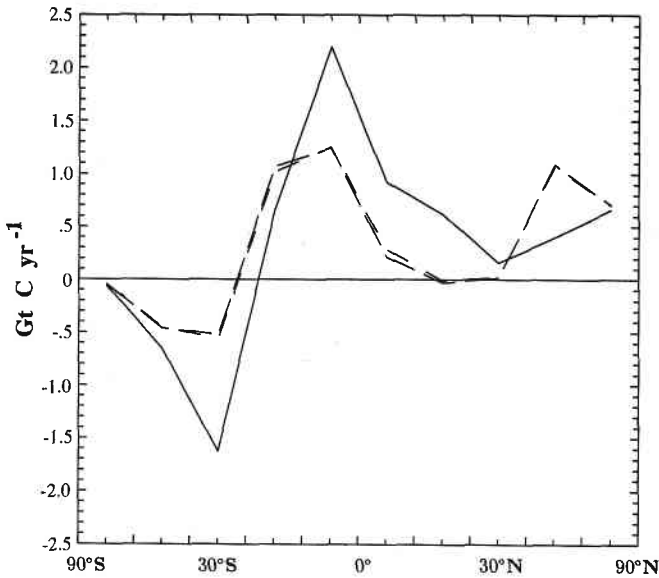
Figure 24: Total annual carbon sources (in Gigatonnes) in each of 10 equal area latitudinal zones. The solid curve refers to the deduced source in the standard run. The broken curve refers to the case where the type C inter-hemispheric gradient has been used instead of the standard one. The dashed curve refers to the case where the type C inter-hemispheric gradient and the alternative (GMCC) seasonal cycle have been used. A, B, C and D refer to the cases where the surface CO_2 observations are taken from the four descriptions of the inter-hemispheric gradient described in the text.

The three figures are qualitatively similar. However, the use of the non-standard (smoother) inter-hemispheric gradient has caused a strengthening of the seasonal cycle in the Northern mid-latitudes while all other seasonal features have been weakened. Figure 24, which shows the annual mean deduced sources for the three sets of results, displays the same broad effects of varying the inter-hemispheric gradient that were considered when discussing Figure 21.

The three sets of deduced sources are quantitatively compared in Table 7. The pattern correlation coefficient and root mean square difference between the standard run, α, and the run with type-C inter-hemispheric gradient, β, are very close to the statistics discussed earlier where the standard run was compared to one with the alternative seasonal cycle — in that case the statistics were 0.964 and 6.49 $Gt/(E^*yr)$ respectively. Run γ employs the variations on both the inter-hemispheric gradient and the seasonal cycle. It is interesting that if the two variations are regarded as perturbations from the standard set of observations, and those perturbations have exactly zero correlation with the standard observations and each other then the pattern correlation coefficient would be 0.935 and the root mean square difference 9.09 $Gt/(E^*yr)$. The actual values in Table 7 are very close to these and so indicate, as would be expected, that there is no significant correlation between the perturbations and the standard set of CO_2 observations.

Experiment	Correlation coefficient	Root mean square diff.	Regression coefficient
$0.9 \times \psi$	0.9993	1.382	0.958
$0.9 \times$ KPP	0.9996	0.924	0.975
$0.9 \times$ KYY	0.9998	0.646	0.982
$0.9 \times$ KYP	0.9999	0.428	1.009
$0.9 \times$ (ψ, all Ks)	0.9995	2.100	0.923
R1	0.9989	1.186	0.994
R2	0.9975	1.796	1.005
R3	0.9966	2.099	0.984

Table 8: Statistics comparing the deduced surface sources in a number of experiments to that in the standard run. The experiments are fully described in the text. The second column gives the correlation coefficient, the third column gives the root mean square difference and the fourth column gives the regression coefficient.

6. Uncertainties in the zonally averaged transport coefficients

The significance of the uncertainties in the transport coefficients was examined by conducting a number of experiments in which the transport coefficients were perturbed. Table 8 lists the statistics comparing the deduced surface sources in these experiments to those in the standard run.

For the first experiment the usual streamfunction is everywhere multiplied by 0.9. For the second experiment it is the vertical diffusion coefficient which is multiplied by 0.9, for the third experiment the horizontal diffusion coefficient, and for the fourth experiment the cross-diffusion term. In the fifth experiment all four coefficients are everywhere multiplied by 0.9.

The deduced source from this last experiment is shown in Figure 25. Note how this figure strongly resembles the standard deduced source, but with the peaks and troughs smoothed out.

The correlation coefficients in the first five rows of Table 8 confirm that, for a uniform decrease in one of the transport coefficients, the deduced sources are very highly correlated with those deduced in the standard case. By contrast, the regression coefficient is very different from 1 in each case (excepting that involving the cross-diffusion term). It is clear that a uniform decrease in the one of the transport coefficients corresponds to an almost uniform decrease in the magnitude of the deduced source. The fifth row of the table shows that a 10% decrease in the transport changes the deduced surface source, as measured by the regression coefficient, by less than 10%. Thus the source is not as sensitive to perturbations in the transport fields as it is to other perturbations, for example those in the surface concentrations.

This may be appreciated intuitively by considering the case of a small change to the transport coefficients. To a first approximation the solution adjusts by proportionally varying the source. This behaviour is suggested by equations 3.9 and 4.2 of Newsam and Enting (1988) in which the source deduction problem is considered for
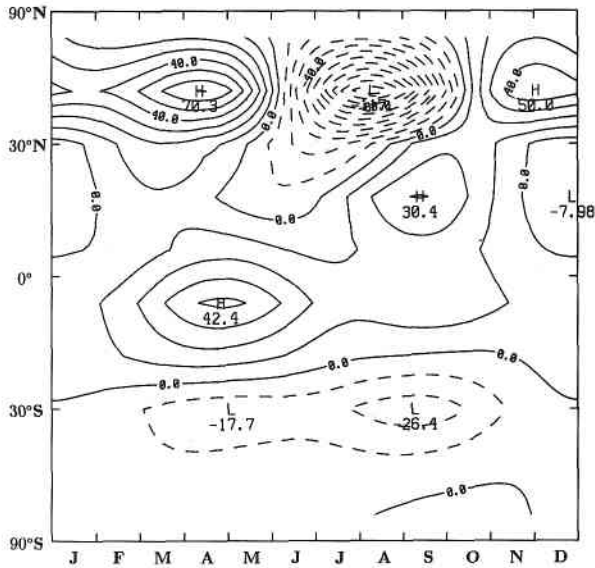
Figure 25: As for Figure 1, but all of the transport coefficients have been multiplied by 0.9.

a simplified model where transport is due to three-dimensional homogeneous turbulence. Those equations show that, in the asymptotic limit of large wave-number, the deduced source changes in proportion to changes made simultaneously to all of the diffusion coefficients.

All three statistics in the first four rows of Table 8 indicate that the largest changes in the deduced source result from changes in the streamfunction. Next important is the vertical diffusion coefficient, followed by the horizontal diffusion coefficient and the cross-diffusion coefficient.

Further experiments were conducted where values X_i were chosen from a zero mean, unit standard deviation, Gaussian distribution. The Fourier coefficients in time for each of the transport coefficients were projected onto the space grid and then multiplied by different factors $(1.0 + 0.1X_i)$. The statistics resulting from three such experiments with random errors are shown in Table 8.

The correlation coefficient and root mean square statistics indicate that the deduced sources for these experiments are less like the standard source than the earlier experiments with a smooth variation of the transport fields but the linear regression coefficient indicates the opposite. This is to be expected when comparing systematic and random errors.

Finally, it should be noted that in some two-dimensional transport models very different transport fields have been used. In EM3 we compared the present model with that of Hyson et al. (1980). This model uses the Eulerian advection fields of Oort (1983) together with diffusion coefficients tuned by Hyson et al. but ultimately derived from Hidalgo and Crutzen (1977). We doubled their horizontal diffusion coefficients in order to simulate the numerical diffusion in their model and then used this transport field to deduce the surface sources in our model. The result is
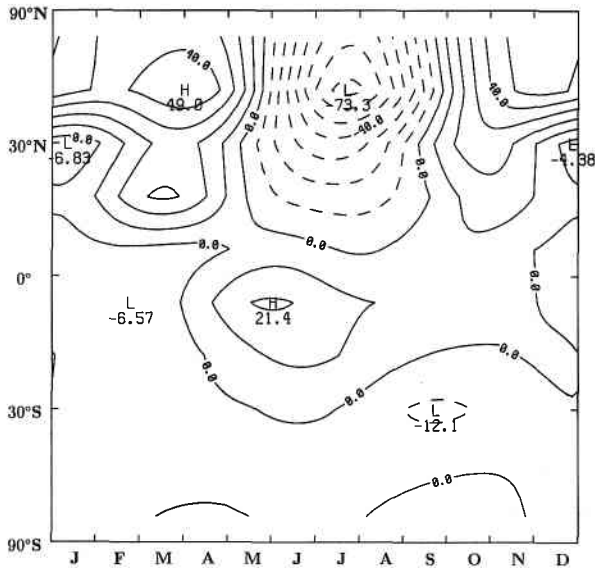
Figure 26: As for Figure 1, but the transport coefficients have been taken from Hyson et al. (1980) with the horizontal diffusion doubled to simulate their numerical diffusion.

shown in Figure 26.

The deduced source in this case is clearly very different from that of the standard run. The correlation coefficient between the two is 0.768 and the root mean square difference is 16.19 Gt/(E*yr). The Hyson et al. fields produce a much weaker set of deduced sources and this is reflected in a linear regression coefficient of 0.637.

7. Errors in projecting the transport coefficients

The transport coefficients derived by Plumb and Mahlman (1987) were calculated as monthly mean values on a grid of 74 points equally spaced in latitude (not counting the poles) and 9 non-equally spaced pressure levels (not counting the upper and lower boundaries). To use these values in the 2-d transport model we first replaced all negative values of the horizontal and vertical diffusion coefficients by zero. We then found the best fit (in the least squares sense) finite Fourier decomposition in time and space for each of the fields. The 100 Fourier coefficients with the largest magnitude were then projected onto the 8×10 grid in space at time intervals of 0.01 years for use in the model.

The exact form of the Fourier decomposition depends on the field being decomposed and the variable used: $t =$ time, $p =$ pressure, $z =$ height or $y = (1 + \sin(\text{latitude})/2)$. The fields used in the standard run were ψ (the velocity streamfunction), KZZ (the vertical diffusion in height coordinates), KYY (the horizontal diffusion in sin(latitude) coordinates) and KYP (the cross-diffusion in y and p coordinates). The vertical coordinates for each field were chosen so that the field would vary as slowly as possible and so allow the best representation by a small set
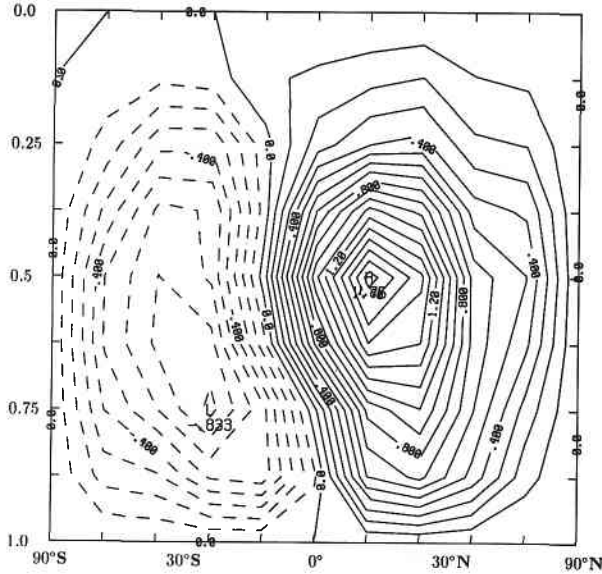
Figure 27: The mid-january mass streamfunction, in atmospheric masses per year, as used in the standard run.

of wavenumbers. Since KPP = p^2 KZZ and the mass streamfunction = $p\psi$ then the coordinate change causes no difficulty when projecting onto the p–y grid.

For the fields employed in the standard run, denoted ψ_s, KZZ_s , KYY_s and KYP_s , we used wavenumbers 1 to 20 for a Fourier sine series expansion in πy and wavenumbers 0 to 2 for a Fourier series expansion in $2\pi t$. KYP and KZZ were expressed as Fourier sine series in πp and KYY was expressed as a Fourier cosine series in πp using wavenumbers 1 to 6 in each case. These choices were determined by the boundary conditions for these fields. Because the velocity streamfunction tended to zero on the lower boundary and a constant on the upper boundary we expressed it as a cosine series in $\pi p/2$ using wavenumbers 1 to 10.

The accuracy of this procedure was tested by creating two alternative sets of fields. In the first we followed the same procedure except that instead of taking a spectral decomposition in the vertical we linearly interpolated the fields onto the pressure grid used in the 2-d model. We give these fields the subscript p. To form the second set of fields we linearly interpolated the Plumb and Mahlman monthly mean fields onto our p–y grid. These field were given the subscript 'pyt'.

The resultant mass streamfunctions at mid-January for the three sets of fields are given in Figures 27, 28 and 29. These Figures give an intuitive sense of the differences in mass flux which result from the different projection methods; Table 9 gives some statistics which quantify these differences.

The statistics compare the first and second named fields. Note that we are comparing the non-dimensionalized fields used directly by the transport model, i.e., the mass streamfunction, KPP, KYY and KYP. The first statistic is the root mean square difference between the two fields using the 960 points made up from the 12 values at the middle of each month projected onto the 8 × 10 grid. The second
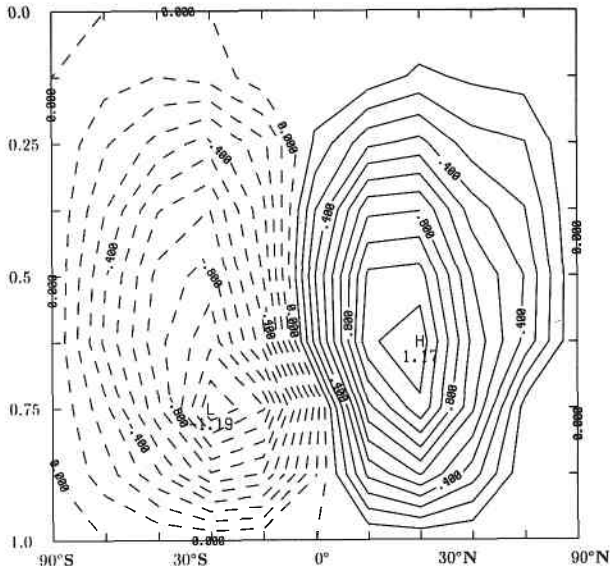
Figure 28: The mid-january mass streamfunction, in atmospheric masses per year, where linear interpolation was used in the vertical.
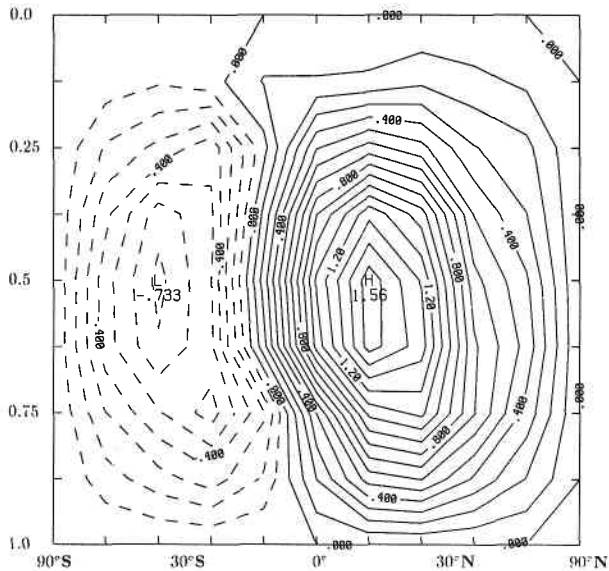

Figure 29: The mid-january mass streamfunction, in atmospheric masses per year, where linear interpolation from the gridded monthly mean values of Plumb and Mahlman (1987) was used.

Field 1	Field 2	RMSD	Total ρ	ρ_1	Total A	A_1
ψ_{pyt}	ψ_{s}	0.104	0.987	0.989	0.955	0.784
ψ_{pyt}	ψ_{p}	0.219	0.954	0.986	0.923	0.944
ψ_{p}	ψ_{s}	0.228	0.949	0.981	0.907	0.810
$\mathrm{KPP}_{\mathrm{pyt}}$	$\mathrm{KPP}_{\mathrm{s}}$	0.367	0.982	0.954	0.934	0.841
$\mathrm{KPP}_{\mathrm{pyt}}$	$\mathrm{KPP}_{\mathrm{p}}$	0.526	0.972	0.957	0.955	0.918
$\mathrm{KPP}_{\mathrm{p}}$	$\mathrm{KPP}_{\mathrm{s}}$	0.518	0.970	0.934	0.976	0.936
$\mathrm{KYY}_{\mathrm{pyt}}$	$\mathrm{KYY}_{\mathrm{s}}$	0.096	0.968	0.977	0.981	0.986
$\mathrm{KYY}_{\mathrm{pyt}}$	$\mathrm{KYY}_{\mathrm{p}}$	0.120	0.942	0.886	0.994	0.997
$\mathrm{KYY}_{\mathrm{p}}$	$\mathrm{KYY}_{\mathrm{s}}$	0.131	0.933	0.899	0.967	0.973
$\mathrm{KYP}_{\mathrm{pyt}}$	$\mathrm{KYP}_{\mathrm{s}}$	0.063	0.994	0.996	0.958	0.948
$\mathrm{KYP}_{\mathrm{pyt}}$	$\mathrm{KYP}_{\mathrm{p}}$	0.140	0.966	0.962	0.984	0.996
$\mathrm{KYP}_{\mathrm{p}}$	$\mathrm{KYP}_{\mathrm{s}}$	0.145	0.967	0.965	0.938	0.949

Table 9: Statistics comparing the first and second named fields. Fields with the subscript s are as used in the standard run (which have been spectrally decomposed in pressure, horizontally and time), those with the subscript p have been linearly interpolated in pressure but spectrally decomposed in the other two dimensions and those with the subscript pyt have been linearly interpolated in all three dimensions. The first statistic is the root mean square difference between the two fields using the 960 points made up from the 12 values at the middle of each month projected onto the 8 × 10 grid. The second statistic is the correlation coefficient using all 960 points and the third statistic is the correlation coefficient using the 120 points on the lowest level above the ground. The fourth statistic is the total regression coefficient A, where (first field) $=$ A×(second field) and the fifth statistic is the regression coefficient A_1 where only the 120 points from the surface concentrations are used.

Fields 1	Fields 2	Correlation coefficient	Root mean square diff.	Regression coefficient
$(\psi_{\mathrm{pyt}}, \mathrm{K}_{\mathrm{pyt}})$	$(\psi_{\mathrm{s}}, \mathrm{K}_{\mathrm{s}})$	0.960	7.090	0.890
$(\psi_{\mathrm{pyt}}, \mathrm{K}_{\mathrm{pyt}})$	$(\psi_{\mathrm{p}}, \mathrm{K}_{\mathrm{p}})$	0.961	6.481	1.025
$(\psi_{\mathrm{p}}, \mathrm{K}_{\mathrm{p}})$	$(\psi_{\mathrm{s}}, \mathrm{K}_{\mathrm{s}})$	0.966	6.951	0.840
$(\psi_{\mathrm{s}}, \mathrm{K}_{\mathrm{p}})$	$(\psi_{\mathrm{s}}, \mathrm{K}_{\mathrm{s}})$	0.985	4.471	0.933
$(\psi_{\mathrm{p}}, \mathrm{K}_{\mathrm{s}})$	$(\psi_{\mathrm{s}}, \mathrm{K}_{\mathrm{s}})$	0.986	4.459	0.914
$(\psi_{\mathrm{p}}, \mathrm{K}_{\mathrm{m}})$	$(\psi_{\mathrm{s}}, \mathrm{K}_{\mathrm{s}})$	0.978	5.902	0.855
$(\psi_{\mathrm{p}}, \mathrm{K}_{\mathrm{m}})$	$(\psi_{\mathrm{p}}, \mathrm{K}_{\mathrm{p}})$	0.997	1.696	1.004

Table 10: Statistics comparing the deduced sources where different sets of transport coefficients have been used. The first statistic gives the correlation coefficient, the second statistic gives the root mean square difference and the third gives the regression coefficient A, where (source from field 1) $=$ A×(source from field 2).
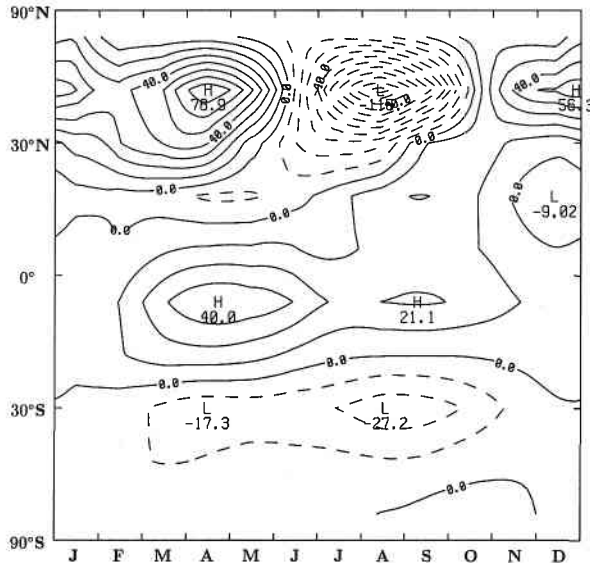
Figure 30: As for Figure 1, but the original monthly mean transport fields of Plumb and Mahlman (1987) have been linearly interpolated onto the standard 8×10 p–y grid to give transport coefficients which are linearly interpolated in time during a source-deduction run of the 2-d transport model.

statistic is the correlation coefficient using all 960 points and the third statistic is the correlation coefficient using the 120 points on the lowest level above the ground. The fourth statistic is the total regression coefficient A, where [first field] $= A \times$ [second field] and the fifth statistic is the regression coefficient A_1 where only the 120 points from the lowest level are used.

The corrrelation coefficients in the table indicate that the projected fields are very similar. Although the correlation coefficients do not indicate that the linear interpolation in p produces a closer fit to the original field than does the spectral fit the linear regression coefficients do indicate this.

Most importantly, the linear regression coefficients suggest that the spectral decomposition causes a systematic overestimation of the transport coefficients. In particular, the mass streamfunction and vertical diffusion coefficients are generally overestimated by more than 10% at the level closest to the ground. This would be expected to result in an overestimate of the magnitude of the deduced source/sink. That this does occur can be seen from Table 10.

The first row in the table compares the deduced source when the transport coefficients are linearly interpolated directly from the Plumb and Mahlman fields (having subscripts 'pyt') with the deduced source found in the standard run (where the transport coefficients have subscript 's'). The linear regression coefficient shows that the deduced source from the standard run has a magnitude about 10% greater than that using the interpolated transport coefficients. This is easily observed by comparing Figure 30, which shows the latter deduced source, with the standard deduced source in Figure 1.

Fields 1	Fields 2	Correlation coefficient	Root mean square diff.	Regression coefficient
(ψ_p, K_p)	(ψ_s, K_s)	0.965	6.411	0.817
(ψ_s, K_p)	(ψ_s, K_s)	0.978	4.984	0.882
(ψ_p, K_s)	(ψ_s, K_s)	0.992	2.933	0.937

Table 11: As for Table 10 except that the source deduction method is not the standard one but involves quadratic interpolation of the CO_2 near the surface. This is fully described in Section 3.

The second row of the table compares the deduced source derived from the fully interpolated fields with those where the interpolation is only in p. This does not indicate any systematic difference between the two deduced sources and so suggests that the choice between linear interpolation and spectral decomposition is important for the vertical coordinates but not the horizontal or time ones.

This conclusion is supported by examination of the third row of the table. Here the sources from the fields with interpolation only in p are compared to those of the standard run. The linear regression coefficient is similar to that in the first row.

Rows four and five of the table give comparisons in which for the first deduced source either the streamfunction or the set of diffusion coefficients has been linearly interpolated in p and the other has not. The linear regression coefficients in the two rows are very similar and so suggest that the systematic difference comes equally from the interpolation in the streamfunction and the diffusion coefficients.

We would expect that most of the systematic error caused by the interpolation of the diffusion coefficients to be due to the vertical term. This is because our earlier results showed that the horizontal and cross diffusion coefficients are not affected by the method of vertical interpolation as much as is the vertical diffusion coefficient. Also we would expect the vertical term to be the dominant one in determining the deduced source at the surface.

This is confirmed by rows 6 and 7 of the table. Here the expression K_m means that the the field of diffusion coefficients is made up of KPP_p , KYY_s and KYP_s, i.e., linear interpolation has been used in the vertical for the vertical diffusion coefficient but spectral decomposition has been used for the other two. Note the strong similarities between the coefficients in rows three and six. The statistics in row seven show directly that the deduced source depends very little on the method by which the KYY and KYP are interpolated vertically.

This importance of the interpolation method is not dependent on the source-deduction method. A series of experiments using a different source deduction procedure have produced comparable results. We employed the third source-deduction method described in Section 3 (involving fitting a parabola to the tracer concentrations) in experiments with different sets of transport coefficients. The results are summarized in Table 11 and the three rows in that table may be directly compared with rows three, four and five in Table 10.

8. Conclusions

Better modelling of the lower boundary is crucial to improving the accuracy with which the surface data, i.e., observations from the surface boundary layer, can be inverted. However, the extent to which the boundary layer can be modelled on a zonally averaged basis is not known.

One possibility for reducing sensitivity to boundary effects is to use non-surface data (both EM3 and Tans et al. have used surface data exclusively). However, Newsam and Enting (1988) have noted that the inversion of upper atmosphere data is much less well conditioned than is the inversion of surface data, due to the sparcity of observations. Moreover, much of the lost information is zonal variation and this will lead to aliasing errors in a zonally averaged model. Thus the use of non-surface data could only determine a small number of modes of variation but it could do so with less ambiguity than could surface data. Numerical experiments along these lines are planned for the future.

As is usual in inverse problems, the result (the surface source) is sensitive both to the observations (the surface concentrations) and the model (the transport coefficients). Plausible variations in the observations and the model have indicated that many details of the deduced sources in the Southern Hemisphere are close to the noise level. However, these changes further weaken the net Southern Hemisphere sink in comparison to the Northern sink and so strengthen the case for the existence of strong non-oceanic sinks in Northern latitudes (as stated in EM3). Similarly, the seasonality of the tropical source (attributed in EM3 to seasonal burning of cleared biomass) seems to be a persistant feature well above the noise level. The seasonal features of the northern hemisphere, having a much larger magnitude than those in the southern hemisphere, are correspondingly much larger than any noise.

References

Enting, I.G. and Mansbridge, J.V., 1986, Description of a two-dimensional atmospheric transport model. *Division of Atmospheric Research Technical Paper* No. 11, (CSIRO, Australia) 22pp.

Enting, I.G. and Mansbridge, J.V., 1987, Preliminary studies with a two-dimensional model using transport fields derived from a GCM. *Division of Atmospheric Research Technical Paper* No. 14, (CSIRO, Australia) 47pp.

Enting, I.G. and Mansbridge, J.V., 1989, Seasonal sources and sinks of atmospheric CO_2: Direct inversion of filtered data. *Tellus* , **41B**, 111-126.

Harris, J.M. and Bodhaine, B.A., 1983, *Geophysical Monitoring for Climatic Change No. 11. Summary Report 1982.* (U.S. Dept. Commerce) 160pp.

Hidalgo, H. and Crutzen, P.J., 1977, The tropospheric and stratospheric composition perturbed by NO_x emissions of high-altitude aircraft. *J. Geophys. Res.,* **82,** 5833-5866.

Hoel, P.G., 1971, *Introduction to Mathematical Statistics (4th edition).* (John Wiley and Sons, New York).

Hyson, P., Fraser, P.J. and Pearman G.I., 1980, A two-dimensional transport simulation model for trace atmospheric constituents. *J. Geophys. Res.,* **85C,** 4443–4455.

Newsam, G.N. and Enting, I.G., 1988, Inverse problems in atmospheric constituent studies: I. Determination of surface sources under a diffusive transport approximation. *Inverse Problems,* **4,** 1037–1054.

Oort, A.H., 1983, Global atmospheric circulation statistics, 1958– 1973. *NOAA Professional Paper* No. 14. (U.S. Dept. Commerce) 180pp plus microfiche.

Plumb, R.A. and Mahlman, J.D., 1987, The zonally averaged tranport characteristics of the GFDL general circulation/transport model. *J. Atmos. Sci.,* **44,** 298–327.

Schnell R.C. and Rosson, R.M., 1986, *Geophysical Monitoring for Climatic Change No. 14. Summary Report 1985* (U.S. Dept. Commerce) 146pp.

Tans, P.P., Conway, T.J. and Nakazawa, T., 1989, Latitudinal distribution of the sources and sinks of atmospheric carbon dioxide derived from surface observations and an atmospheric transport model. *J. Geophys. Res.,* **94D,** 5151–5172.